OEA | Opto-Electronic Advances

Article

February 2026, Vol. 9, No. 2

Open Access

Ambient-energy-driven space-time-coding metasurface for space-frequency-division multiplexing wireless communications

Han Wei Tian[1], Chao Song[1], Dong Jie Wang[1], Qian Zhu[1], Tie Jun Cui[1]* and Wei Xiang Jiang[1,2]*

Abstract: Programmable metasurfaces have shown exceptional potentials in wireless communications due to their capability to manipulate electromagnetic (EM) waves dynamically and flexibly. However, the large-scale application and flexible deployment of programmable metasurfaces still face challenges of high communication capacity requirements and stringent energy constraints. Here, we report an ambient-energy-driven space-time-coding metasurface to address these issues. On one hand, the metasurface can achieve efficient space-frequency-division multiplexing manipulations by dynamically controlling multiple frequencies and the spatial propagation directions of reflection EM waves. On the other hand, the shared-aperture ambient solar energy harvesting capability and low power consumption characteristic of the metasurface enable it to be self-powered without relying on any external power supply. To demonstrate these remarkable features, a four-channel wireless communication system prototype is built using the programmable metasurface. Experimental results confirm that four distinct images can be transmitted to four user terminals simultaneously, independently, and in real time with remarkably low energy consumption per bit. Such innovative metasurface provides a simple and effective approach for integrating ambient energy harvesting, multi-dimensional microwave manipulation, and direct information modulation on a single physical platform, which will advance the wireless communications in cost-effectiveness, enhanced capacity, energy efficiency, and environmental friendliness.

Keywords: programmable metasurfaces; space-time-coding metasurfaces; ambient energy harvesting; self-powered; multiplexing wireless communications; energy-efficient

DOI: 10.29026/oea.2026.250229 | CSTR: 32247.14.oea.2026.250229

Citation: Tian HW, Song C, Wang DJ et al. Ambient-energy-driven space-time-coding metasurface for space-frequency-division multiplexing wireless communications. *Opto-Electron Adv* **9**, 250229 (2026).

1 Introduction

The envisioned next-generation wireless networks aspire to provide ubiquitous connectivity for a massive users and ultra-dense Internet of Things devices while delivering superior communication service quality[1–3]. However, achieving the new paradigm shift requires to increase the deployment density and breadth of wireless communication infrastructures (e.g., base stations and relays) significantly, which will inevitably lead to a continuous increase in energy consumption, operating costs and system complexity. Therefore, simple, energy-efficient and cost-effective wireless communication architectures have become a key research frontier to reconcile these conflicts. Programmable metasurfaces (PMs), also termed as reconfigurable intelligent surfaces (RISs), have emerged as a transformative solution due to their ability to freely and flexibly manipulate electromagnetic (EM) waves, complemented by advantages such as low cost, low complexity, and high integrability[4–11]. The current studies leverage PMs through two principal paradigms: 1) passive relaying surfaces that optimize the channel quality through spatial beamforming[12–15], and 2) simple-architecture wireless communication systems that directly modulate information on scattered EM waves[16–19].

Recent studies have also realized various multiplexing communication systems, such as frequency-division

Received: 31 August 2025

Accepted: 16 December 2025

Published online: 4 February 2026

[1]State Key Laboratory of Millimeter Waves, School of Information Science and Engineering, Southeast University, Nanjing 210096, China; [2]Purple Mountain Laboratories, Nanjing 211111, China.
*Correspondence: TJ Cui, E-mail: tjcui@seu.edu.cn; WX Jiang, E-mail: wxjiang81@seu.edu.cn

multiplexing communications based on dual-frequency/time-domain PMs[20–22], and space-division multiplexing communication systems through PM-based multi-beamforming[23–27]. Such advancements further highlight the potential of PMs in enhancing the communication capacity. Multi-dimension-division multiplexing communication systems have further been implemented using space-time-coding metasurfaces (STCMs), including space-frequency-division multiplexing communications and space-frequency-polarization-division multiplexing communications[28–31]. However, the current STCM-based multi-dimension-division multiplexing communication systems have a notable limitation, namely redundant use of limited EM resources. For example, at least two different spatial propagation directions and two different frequencies, or two orthogonal polarizations and two frequencies, were required to realize two independent information transmission channels. Therefore, developing a multiplexing communication strategy that can more efficiently utilize limited EM resources to expand the number of information transmission channels is crucial to further improve the system communication capacity.

On the other hand, stringent energy constraints of next-generation wireless networks constitute a pivotal challenge to the flexible and scalable deployment of PMs. Current energy-saving solutions on PMs focus on adopting low-power electronic components such as radio frequency (RF) switches but neglect substantial energy overhead from the back-end control circuits[32,33], particularly field-programmable gate arrays (FPGAs) and any other power-hungry peripheral components. In addition, PMs using application-specific integrated circuits (ASICs) can localize control functions to individual meta-atoms, thereby reducing the overall power consumption by eliminating the need for peripheral circuits[34,35]. However, ASIC implementations necessitate customized circuit architecture tightly coupled to specific PM geometries, limiting flexibility and adaptability across diverse PM geometries and application scenarios. Another viable strategy is to build PMs that can autonomously harvest energy from the surrounding environment. Several PM prototypes have been proposed and demonstrated their capability to be self-powered by directly harvesting ambient energy (e.g., RF/solar/mechanical energy)[36–40]. However, all current studies simply integrate external energy harvesting devices (e.g. rectifier circuits, large-area solar panels, or rotary triboelectric nanogenerators) with programmable metasurfaces. Such crude integration method severely affects their EM wave manipulation and energy harvesting performance, as well as their compactness and array scalability. In addition, relevant studies are still in their infancy and mainly focus on the realization of autonomous energy harvesting and energy self-sufficiency, and their potential for simultaneously realizing dynamic beamforming and direct information modulation remains to be explored.

Motivated by above challenges, we propose an ambient-energy-driven STCM (ASTCM) by heterogeneously integrating a solar cell chip (SCC) onto each meta-atom to achieve the dynamic control of reflected EM waves and harvest ambient solar energy through sharing the same physical aperture, as illustrated in Fig. 1. Various space-time-coding (STC) matrixes are optimized for ASTCM to effectively generate multiple reflected EM harmonics and perform multi-beamforming on these harmonic frequencies independently. This feature lays the foundation for efficiently constructing multiple independent information transmission channels through space-frequency-division multiplexing manipulation. By modulating the phase of each reflection beam independently, distinct digital information can be transmitted directly and concurrently, without interference through these wireless channels to different user terminals. On the other hand, a solar power management circuit (SPMC) is integrated to ASTCM, which empowers efficient storage and use of the harvested ambient solar energy. Both ASTCM and its backend control circuit adopt low-power design strategies, which not only ensures the high energy efficiency, but also facilitates the practical implementation of autonomous power supply. As a proof-of-concept, an ASTCM prototype and a four-channel wireless communication system prototype are designed to verify the above features. Compared to previous metasurfaces, the ASTCM concept opens up an avenue for achieving energy harvesting, microwave manipulation, and information modulation using a unified physical platform, offering a promising solution for next-generation wireless networks.

2 Results and discussion

2.1 Meta-atom design of ASTCM and its microwave modulation performance

To realize the above concept, we first tactfully design an ASTCM by integrating SCCs, whose meta-atom structure is shown in Fig. 2(a). The meta-atom is a dual-layer structure containing the phase modulation layer and the energy harvesting layer. As depicted in Fig. 2(b), the phase modulation layer is constructed by etching a rectangular patch and two bias lines on the F4BM220 substrate (dielectric constant ε_r = 2.2, loss tangent tanσ = 0.001, thickness h_1 = 1.5 mm), and two low-power single-pole single-throw (SPST) switches are loaded at two gaps between the rectangular patch and bias lines. A metallized via is introduced to connect the rectangular patch and the metallized ground on the back of the substrate, which not only provides bias ground for SPST switches, but more importantly, it breaks the geometric symmetry of the phase modulation layer and therefore ensures that the meta-atom achieves 2-bit reflection phase modulation by tuning the two SPST switches. As shown in Fig. 2(c), the substrate of the energy harvesting layer is F4BM265 (dielectric constant ε_r = 2.65, loss tangent tanσ =

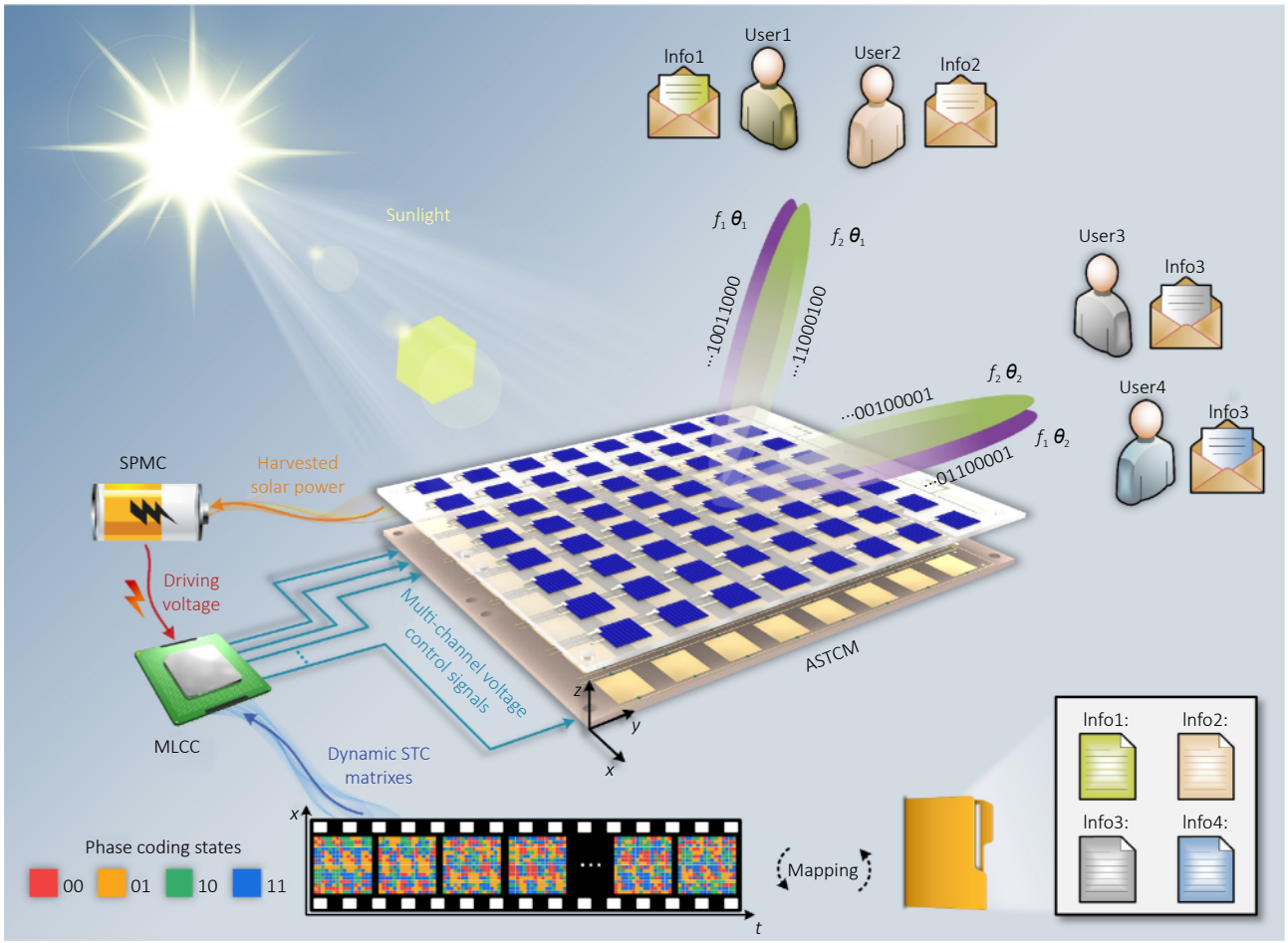


Fig. 1 | Conceptual illustration of ASTCM. The ASTCM features a dual-layer structure, comprising a phase modulation layer (the bottom layer) and an energy harvesting layer (the upper layer). By further integrating SPMC and MLCC, ASTCM can be entirely powered by the ambient solar energy it harvests. Additionally, through the optimization of various STC matrices, ASTCM can perform independent multi-beamforming at multiple frequencies, thus achieving multi-channel information transmission via efficient space-frequency division multiplexing. SPMC: solar power management circuit, MLCC: microcontroller-based low-power control circuit.

0.0015, thickness h_2 = 1.5 mm). A rectangular patch with a direct current (DC) line is etched on the top of the substrate, and another DC line is etched on the back. To enable ambient solar energy harvesting via a shared aperture, a triple-junction gallium arsenide (GaAs) SCC is directly integrated in the energy harvesting layer on each meta-atom, and its cross-sectional structure is shown in Fig. 2(d). This triple-junction GaAs SCC features a multi-layer stacked structure that harvest different spectra of sunlight through different layers, thereby achieving high-efficiency wide-spectrum photoelectric conversion. More details of the triple-junction GaAs SCC are provided in Supplementary information of Section 1. The anode of the triple-junction GaAs SCC is attached to the top rectangular patch, while its cathode is connected to the bottom DC line through a SCC-specific aluminum welding stripe and a metallized via. To promise simultaneous reflection microwave modulation and ambient solar energy harvesting, the energy harvesting layer is placed in front of the phase modulation layer with a distance of h_{air} = 2 mm. When the energy harvesting layer is illuminated by sunlight, the integrated SCCs directly convert the sunlight into DC energy and transmit it through DC lines to the back-end SPMC for storage. In addition, the integrated SCCs and metal patches together act as parasitic patches of the phase modulation layer, ensuring that the incident microwave is effectively coupled to the phase modulation layer and vice versa, also ensuring that the reflection microwave can be effectively coupled into the free space. It is noteworthy that the influence of the energy harvesting layer is already well considered in the whole meta-atom design, ensuring that desired reflection microwave modulation performance can be maintained after integrating SCC (see Supplementary information of Section 2 for more details).

To evaluate the reflection microwave modulation performance of the proposed meta-atom, full-wave simulations are conducted with commercial software CST Microwave

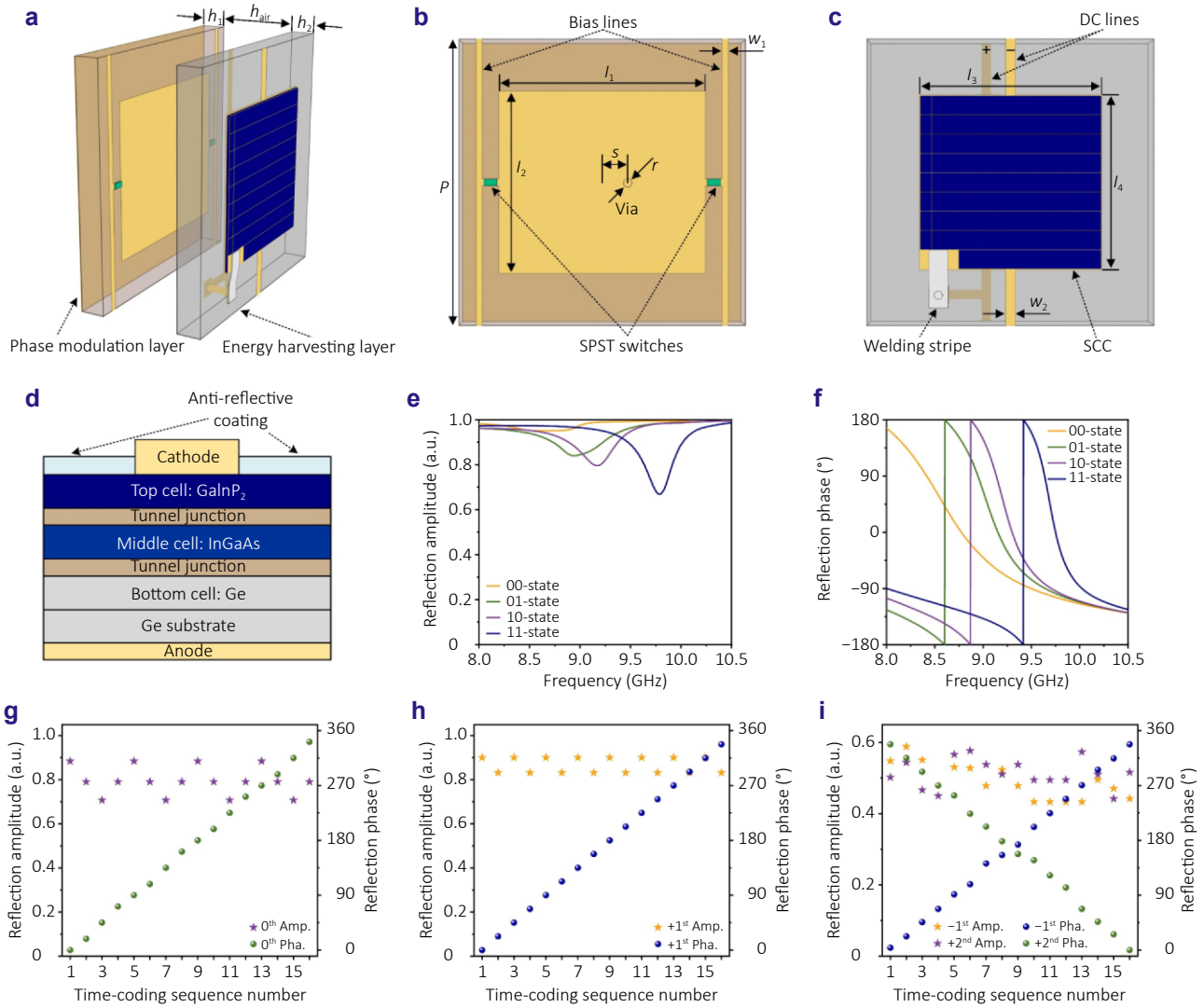


Fig. 2 | Design details of ASTCM and its microwave modulation performance. (a) Geometry of the ASTCM meta-atom. (b) Top view of the phase modulation layer. (c) Top view of the energy harvesting layer. The optimized geometric parameters of each meta-atom are as follows: h_1 = 1.5 mm, h_{air} = 2 mm, h_2 = 1.5 mm, P = 15 mm, l_1 = 10.75 mm, l_2 = 9.5 mm, l_3 = 9.4 mm, l_4 = 9 mm, w_1 = 0.3 mm, w_2 = 0.5 mm, s = 1.3 mm, r = 0.2 mm. (d) Side view of the triple-junction GaAs SCC. $GaInP_2$: gallium indium phosphide, InGaAs: indium gallium arsenide, Ge: germanium. (e) Reflection amplitudes of the ASTCM meta-atom. (f) Reflection phases of the ASTCM meta-atom. (g) The equivalent 4-bit phases and corresponding amplitudes at the fundamental frequency. (h) The equivalent 4-bit phases and corresponding amplitudes at the +1st harmonic. (i) The equivalent 4-bit phases and corresponding amplitudes at both the −1st and +2nd harmonics.

Studio. As depicted in Fig. 2(e, f), by independently controlling the ON/OFF states of the two SPST switches, 2-bit phase modulation can be achieved at 9 GHz, and the reflection amplitudes corresponding to the four phase coding states are all greater than 0.8. Furthermore, we adopt the time-coding method to further improve the microwave modulation capability. When the metasurface is illuminated by a monochromatic microwave incidence with the frequency of f_c and controlled by a periodic time-coding sequence (with the time period of $T_0 = t_0 \times L$, where t_0 is the time slot, L is the sequence length), it will generate a series of reflection microwave harmonics with frequencies of $f_c + mf_0$ (m = 0, ±1, ±2, ±3, ... , $f_0 = 1 / T_0$). Specifically, the equivalent reflection amplitude a^m and phase φ^m of the m^{th} harmonic can be expressed as

$$a^m e^{-j\varphi^m} = \sum_{l=1}^{L} \frac{a_l e^{-j\varphi_l}}{L} \mathrm{sinc}\left(\frac{\pi m}{L}\right) e^{-j\pi m \frac{2l-1}{L}}, \qquad (1)$$

where a_l and φ_l are the basic reflection amplitude and phase in the l^{th} time slot, respectively. It can be observed from Eq. (1) that the equivalent reflection coefficient of the m^{th} harmonic is the superposition of the basic reflection coefficients in a time period. Therefore, here we develop a time-coding strategy based on the particle swarm optimization

algorithm, aiming to achieve efficient generation and full-phase synthesis of any desired reflection microwave harmonic by optimizing the time-coding sequence. Without loss of generality, here we assume that the metasurface generates p (p = 1, 2, ... , P) distinct reflection microwave harmonics and independently modulate their phases, and the fitness function can be expressed as

$$fitness = w_1 \times \sum_{p}^{P} \left| a_{\mathrm{d}}^{m_p} - a_{\mathrm{c}}^{m_p} \right| + w_2 \times \sum_{p}^{P} \left| \varphi_{\mathrm{d}}^{m_p} - \varphi_{\mathrm{c}}^{m_p} \right| , \quad (2)$$

where m_p is the order of the p^{th} harmonic, $a_{\mathrm{d}}^{m_p}$ are $\varphi_{\mathrm{d}}^{m_p}$ are the desired amplitude and phase of the m_p^{th} harmonic, $a_{\mathrm{c}}^{m_p}$ and $\varphi_{\mathrm{c}}^{m_p}$ are the current amplitude and phase of the m_p^{th} harmonic, w_1 and w_2 are weight factors (see Supplementary information of Section 3 for more details on the optimization process of the time-coding sequence). As a verification, two groups of 16 different time-coding sequences are first optimized to achieve equivalent 4-bit phase modulation at the fundamental frequency f_{c} (i.e., m = 0) and the -1^{st} harmonic f_{c}–f_0, respectively. As shown in Fig. 2(g, h), all synthesized equivalent phases match well with the desired phase values (with the phase deviation of less than 4.1°), and the equivalent amplitudes of the fundamental and -1^{st} harmonic frequencies are greater than 0.7 and 0.83, respectively. These results well demonstrate the ability to efficiently generate any desired reflection microwave harmonic as well as accurately modulate its phase. In addition, independent and simultaneous equivalent 4-bit phase modulation at the -1^{st} and $+2^{\mathrm{nd}}$ harmonics is further realized. As displayed in Fig. 2(i), by applying 16 different optimized time-coding sequences, equivalent 4-bit phases can be synthesized at both -1^{st} and $+2^{\mathrm{nd}}$ harmonics (with the deviation from the desired phase values of less than 10°). The phase gradients at the two harmonics show increasing and decreasing trends respectively, indicating that simultaneous and independent phase modulation at multiple frequencies can be achieved. In addition, the equivalent amplitudes of the two harmonics remain at around 0.5, proving the capability of efficient generation of multiple harmonics.

2.2 Realization of ASTCM and its energy harvesting and self-powering performance

As shown in Fig. 3(a), a metasurface array prototype consisting of 16 × 8 meta-atoms is fabricated using the standard printed circuit board technology. To facilitate the integration of SCCs, four metasurface subarrays consisting of 4×8 meta-atoms are first fabricated. After integrating SCCs on each subarray, the four subarrays are then spliced together to form a complete metasurface array. Photos of the phase modulation layer and the energy harvesting laye of each meta-atom are illustrated in Fig. 3(b, c). Then, a SPMC and a microcontroller-based low-power control circuits (MLCC) are further designed and integrated with the metasurface array to construct the final ASTCM, as shown in Fig. 3(d). Notably, meta-atoms in the same column (along the y-direction) of the phase modulation layer share two independent bias voltages to achieve independent control of the two columns of SPST switches. Therefore, the metasurface array enables one-dimensional phase modulation (along the x-direction) in the space domain. In addition, by designing the DC line routing of the energy harvesting layer, the SCCs on each subarray are connected in parallel and the SCCs between different subarrays are connected in series. This configuration ensures that the photovoltage output by the metasurface array matches the input voltage range of the SPMC, thereby allowing the efficient storage of the harvested solar energy. To improve the solar energy harvesting efficiency, the SPMC is designed based on the maximum power point tracking (MPPT) technology, which helps the ASTCM to dynamically adapt to the fluctuations of the ambient solar irradiance and therefore ensuring the real-time maximization of the harversted energy. Meantime, low-power design strategies are adopted to improve the energy self-sufficiency peformance, including the usage of low-power SPST switches (Archiwave, ARW3172) in the metasurface array design as well as low-power MCU (STMicroelectronics, STM32H743) in the MLCC design. To clearly demonstrate the working mechanism of the ASTCM for solar energy harvesting and self-powing, a simplified equvient circuit schematic is shown in Fig. 3(e). It can be observed that the solar energy harvested by the energy harvesting layer is first stored in the SPMC and then output as a stable driving voltage to drive the MLCC. Finally, the MLCC outputs multiple independent voltage signals to tune the SPST switches loaded on the phase modulation layer.

To further evaluate the realistic solar energy harvesting performance of the ASTCM, we utilize a self-made solar simulator to provide artificial sunlight with controllable irradiance (see Materials and methods for more details). Figure 3(f) shows the measured current-voltage (I-V) and power-voltage (P-V) responses of the ASTCM under different sunlight irradiances. It can be observed that as the sunlight irradiance increases, the solar energy harvested by the ASTCM gradually increases. Under the nominal sunlight irradiance of 100 mW/cm^2, the solar energy harvested per unit area of the ASTCM can reach 12 mW/cm^2. Moreover, we measured the power consumption of the ASTCM to evaluate its energy self-sufficiency performance. When all SPST switches are in the ON state, the metasurface array reaches the maximum power consumption, which is measured to be 12.8 mW. We also measured the dynamic power consumption of the MLCC when its 32 channels simultaneously output 1 MHz square wave signals, which is about 177 mW. Hence, the maximum power consumption per unit area of the entire ASTCM can be calculated as 0.66 mW/cm^2, which is much lower than the solar energy it can harvest. Through straightforward estimation, it can be obtained that the ASTCM can harvest enough ambient solar energy to ensure

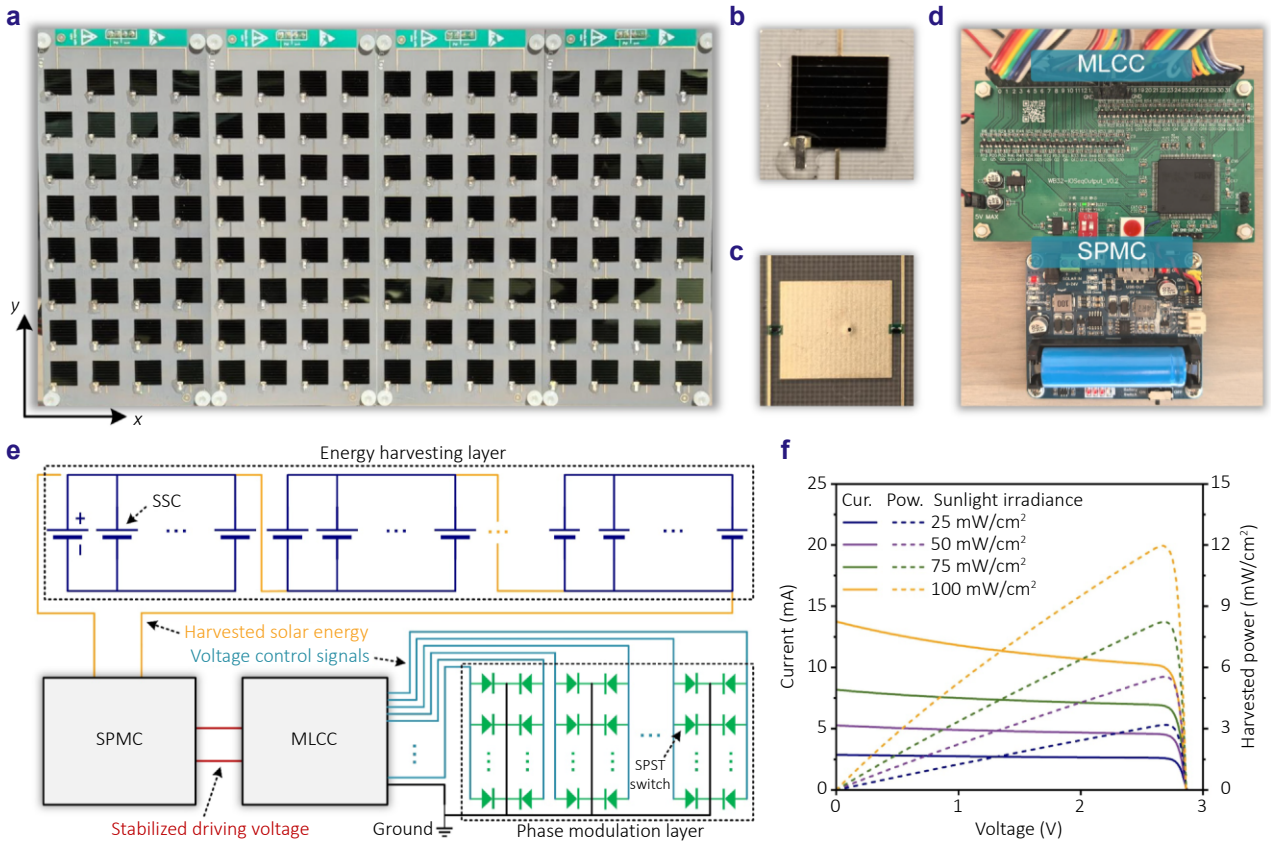


Fig. 3 | Implementation of ASTCM and its solar energy harvesting performance. (a) Photograph of the fabricated ASTCM array prototype. (b) Zoomed view of the energy harvesting layer of the ASTCM meta-atom. (c) Zoomed view of the phase modulation layer of the ASTCM meta-atom. (d) Photograph of the designed MLCC and SPMC. (e) Simplified equivalent circuit schematic of ASTCM for illustrating the solar energy harvesting and self-powering process. (f) Measured *I-V* and *P-V* responses of ASTCM.

it uninterrupted operation for 24 hours under the nominal sunlight irradiation for only about 1.3 hours. It is also worth mentioning that benefit from the 3145 mWh lithium battery integrated in the SPMC, the ASTCM enables continuous operation for approximately 16.6 hours with its stored energy, ensuring robustness in practical scenarios without sunlight input, such as at night and in severe weather (such as rain, snow, fog, etc.).

2.3 Demonstration of independent multi-beamforming at multiple frequencies

Since the realized ASTCM can be programmed in both the frequency and space domains, we further develop a STC strategy to achieve multi-beamforming at any desired frequency. According to the superposition theorem, the multi-beam farfield pattern can be synthesized by superpositing multiple single-beam farfield patterns. When ASTCM is programmable in one dimension, we assume that it is a linear array with N meta-atoms to generate a total of I main beams. Then the single-beam farfield pattern $f^i(\theta)$ corresponding to the i^{th} (i = 1, 2, ... , I) main beam can be expressed as,

$$f^i(\theta) = \sum_{n=1}^{N} f^u(\theta)\, a_n^i \mathrm{e}^{-\mathrm{j}\varphi_n^i} \mathrm{e}^{-\mathrm{j}nkd\sin\theta}\,, \tag{3}$$

where $f^u(\theta)$ is the farfield pattern of the meta-atom, a_n^i and φ_n^i are the amplitude and phase of the n^{th} meta-atom respectively, and k is the wave number. When the i^{th} beam points to θ_{r}^i, we can obtain $\varphi_n^i = nkd\sin\theta_{\text{r}}^i$. Then, the multi-beam farfield pattern can be synthesized as,

$$f(\theta) = \sum_{i=1}^{I} f^i(\theta)\, \mathrm{e}^{\mathrm{j}\varphi_0^i}\,, \tag{4}$$

where φ_0^i is the initial phase of the i^{th} beam. For simplicity, we assume that ASTCM has the ideal reflection amplitude distribution (i.e., $a_n^i = 1$). According to Eq. (2), the desired phase ϕ_n of the n^{th} meta-atom can be expressed as,

$$\phi_n = \arg\left(\sum_{i=1}^{I} \mathrm{e}^{-\mathrm{j}\left(nkd\sin\theta_{\text{r}}^i - \varphi_0^i\right)}\right)\,. \tag{5}$$

Then by combining Eqs. (2) and (5), the time-coding sequence for each meta-atom can be respectively optimized, and finally, the required STC matrix can be obtained by combining these optimized time-coding sequences (see

Supplementary information of Section 4 for more details on the design process of the STC matrix). In addition, by substituting the equivalent amplitude and phase distributions of the ASTCM after applying the STC matrix into Eqs. (3) and (4), the multi-beam farfield pattern generated on the desired harmonic can be calculated.

To further verify the effectiveness of the proposed STC strategy, we performed several dual-beamforming experiments. In these experiments, the configuration parameters are set as follows: f_c = 9 GHz, t_0 =1 μs, L = 16 and f_0 = 62.5 kHz. The first experimental scenario is to generate two main beams pointing to −18° and 24° at the fundamental frequency. Figure 4(a) shows the corresponding optimized STC matrix, and Fig. 4(b, c) record the equivalent amplitude and phase distributions of ASTCM from −5th to 5th harmonics after applying the STC matrix. We note that the equivalent amplitude at the fundamental frequency exceeds 0.7, while the equivalent amplitudes at other harmonics are suppressed below 0.15. An equivalent phase distribution with 4-bit resolution is achieved at the fundamental frequency, and it matches the expected phase distribution well (with the maximum phase deviation of less than 4.2°). In addition, both the calculated and measured farfield patterns are illustrated in Fig. 4(d). The measured results are in good agreement with the calculated ones, demonstrating the capability of ASTCM for multi-beamforming at the fundamental frequency. The second experimental scenario is to generate two main beams pointing to −24° and +34° at

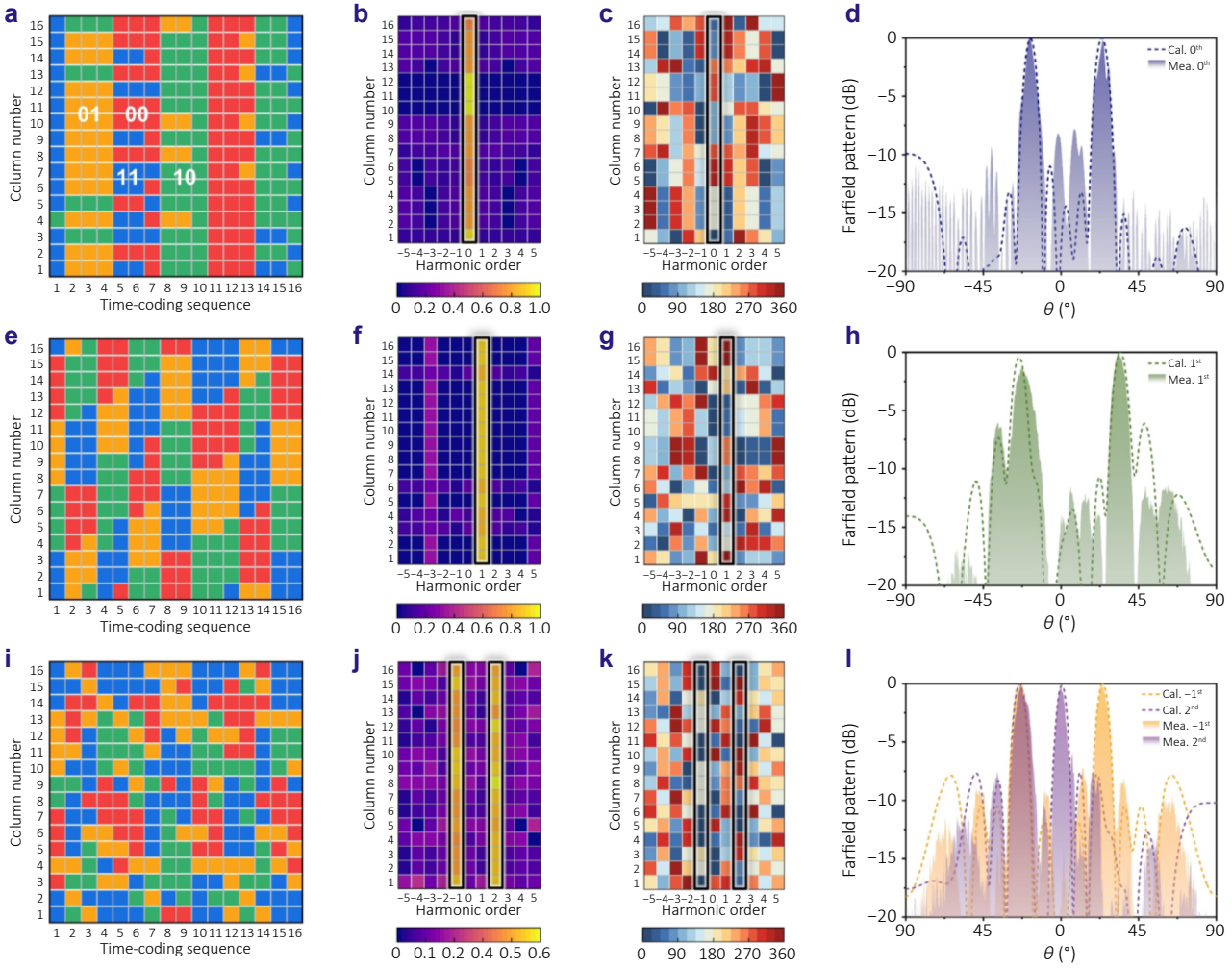


Fig. 4 | Demonstration of independent multi-beamforming at multiple frequencies. (a) Optimized STC matrix for dual-beamforming at the fundamental frequency. (b) Equivalent amplitude distribution and (c) equivalent phase distribution of ASTCM from −5th to 5th harmonics corresponding to dual-beamforming at the fundamental frequency. (d) Calculated and measured farfield patterns of dual-beamforming at the fundamental frequency. (e) Optimized STC matrix for dual-beamforming at the +1st harmonic. (f) Equivalent amplitude distribution and (g) equivalent phase distribution of the ASTCM from −5th to 5th harmonics corresponding to dual-beamforming at the +1st harmonic. (h) Calculated and measured farfield patterns of dual-beamforming at the +1st harmonic. (i) Optimized STC matrix for independent dual-beamforming at both −1st and +2nd harmonics. (j) Equivalent amplitude distribution and (k) equivalent phase distribution of ASTCM from −5th to 5th harmonics corresponding to dual-beamforming at both −1st and +2nd harmonics. (l) Calculated and measured farfield patterns of dual-beamforming at both −1st and +2nd harmonics.

the $+1^{st}$ harmonic ($f_{+1} = f_c + f_0$ = 9.0000625 GHz), and the corresponding optimized STC matrix is shown in Fig. 4(e). After applying this STC matrix, as depicted in Fig. 4(f), ASTCM can efficiently reflect the $+1^{st}$ microwave harmonic with the equivalent amplitude greater than 0.87. In addition, the equivalent phase distribution is completely consistent with the desired phase distribution, as shown in Fig. 4(g). The corresponding calculated and measured farfield patterns are also in good agreement, as illustrated in Fig. 4(h), incidating that ASTCM can achieve multi-beamforming at harmonic frequencies. The third experimental scenario is to perform independent dual-beamforming at both the -1^{st} harmonic ($f_{-1} = f_c - f_0$ = 8.9999375 GHz) and the $+2^{nd}$ harmonic ($f_{+2} = f_c + 2f_0$ = 9.000125 GHz). The corresponding optimized STC matrix, the equivalent amplitude and phase distributions of ASTCM are presented in Fig. 4(i–k), respectively. It can be observed that the equivalent amplitudes of the -1^{st} and $+2^{nd}$ harmonics are significantly higher than that of the other harmonics, while the equivalent phase distributions at the two harmonics are distinct and thus result in different dual-beamforming effects. As shown in Fig. 4(l), the two main beams at the -1^{st} harmonic point to ±24°, while the two main beams at the $+2^{nd}$ harmonic point to −24° and 0°, respectively. Calculated results at both harmonics are in good agreement with the measured results, demonstrating the ability of ASTCM to perform independent multi-beamforming at multiple frequencies.

2.4 Construction of multiple independent information transmission channels

We can generate multiple beams with different frequencies and spatial propagation directions based on ASTCM to construct multiple independent information transmission channels. Without loss of generality, here we illustrate the process of constructing four independent information transmission channels by performing independent dual-beamforming on two different frequencies. Specifically, we use ASTCM to simultaneously generate dual beams pointing to ±24° at the -2^{nd} and $+3^{rd}$ harmonics. Each of the four main beams supports an independent information transmission channel, and different channels are distinguished by different frequencies or spatial propagation directions. For clarity, we name the four channels as CH1 ($f_{-2} = f_c - 2f_0$, $\theta_r^1 = -24°$), CH2 ($f_{+3} = f_c + 3f_0$, $\theta_r^2 = -24°$), CH3 ($f_{-2} = f_c - 2f_0$, $\theta_r^3 = 24°$) and CH4 ($f_{+3} = f_c + 3f_0$, $\theta_r^4 = 24°$). It is notable that each main beam has an independent initial phase, as can be observed from Eq. (4), which lays the foundation for independent phase modulation on each channel. Considering that each single-beam farfield pattern has low amplitude at other main beam directions, modulating the initial phase of any main beam has little effect on both the amplitude and phase of other main beams in the synthesized multi-beam farfield pattern. Therefore, it can be approximately considered that the phase modulation of each main beam does not interfere with each other. Based on this method, each information transmission channel can simultaneously transmit distinct digital information through quaternary phase shift keying (QPSK) modulation scheme by performing independent 2-bit phase modulation on each main beam.

A series of STC matrices M_{ijpq} are optimized to realize independent 2-bit phase modulations of the four channels, where i, j, p, q represent the indexs of CH1, CH2, CH3, and CH4, respectively. These indexs take values of 1, 2, 3, and 4, which refer to the 2-bit phase coding states of "00", "01", "10", and "11" respectively. For instance, we can implement 2-bit phase modulation only on CH1 by applying four optimized STC matrices $\boldsymbol{M}_{1111}$, $\boldsymbol{M}_{2111}$, $\boldsymbol{M}_{3111}$ and $\boldsymbol{M}_{4111}$. Figure 5(a, c) illustrate the farfield patterns generated by the ASTCM at -2^{nd} and $+3^{rd}$ harmonics after applying these four STC matrices. It is evident that main beams pointing to ±24° are generated at both two harmonics. The gain fluctuation of all main beams does not exceed 1 dB, and the beam pointing fluctuation does not exceed 1°. As further shown in Fig. 5(b, d), only the main beam of CH1 produces four different phases of 26.3°, 114.1°, 204.8°, and 292.4°, which correspond to "00", "01", "10" and "11" phase coding states of CH1. The phase difference between adjacent phase states is 90°±2.4°, indicating that 2-bit phase modulation is well achieved. At the same time, the main beam phases of CH2, CH3, and CH4 are almost unchanged, indicating that other channels are not affected by the phase modulation of CH1. Here, we regard the current phases of CH2, CH3, and CH4 as their respective "00" phase coding states. In addition, we can optimize more STC matrices to achieve 2-bit phase modulation only on CH2, CH3, and CH4, respectively. When four optimized STC matrices $\boldsymbol{M}_{2122}$, $\boldsymbol{M}_{2222}$, $\boldsymbol{M}_{2322}$ and $\boldsymbol{M}_{2422}$ are applied, only 2-bit phase modulation can be obtained on CH2, while the main beam phases of CH1, CH3 and CH4 are all in their respective "01" phase coding states, as shown in Fig. 5(e–h). Similarly, as depicted in Fig. 5(i–l), when we apply four optimized STC matrices $\boldsymbol{M}_{3313}$, $\boldsymbol{M}_{3323}$, $\boldsymbol{M}_{3333}$ and $\boldsymbol{M}_{3343}$, only CH3 achieves 2-bit phase modulation, and the phase coding states of CH1, CH2 and CH4 are all "10". Furthermore, when we apply four optimized STC matrices $\boldsymbol{M}_{4441}$, $\boldsymbol{M}_{4442}$, $\boldsymbol{M}_{4443}$ and $\boldsymbol{M}_{4444}$, 2-bit phase modulation is only achieved on CH4, and the phase coding states of CH1, CH2 and CH3 are maintained at "11", as illustrated in Fig. 5(m–p). These results well verify the capability of ASTCM to efficiently construct four independent information transmission channels by only multiplexing two frequencies and two spatial propagation directions of the refection EM waves, and details of all optimized STC matrices mentioned above can be found in Supplementary information of Section 5. It is worth mentioning that more information transmission channels and diverse modulation schemes can be achieved based on the proposed ASTCM. As a demonstration, we further provide a six-channel case by

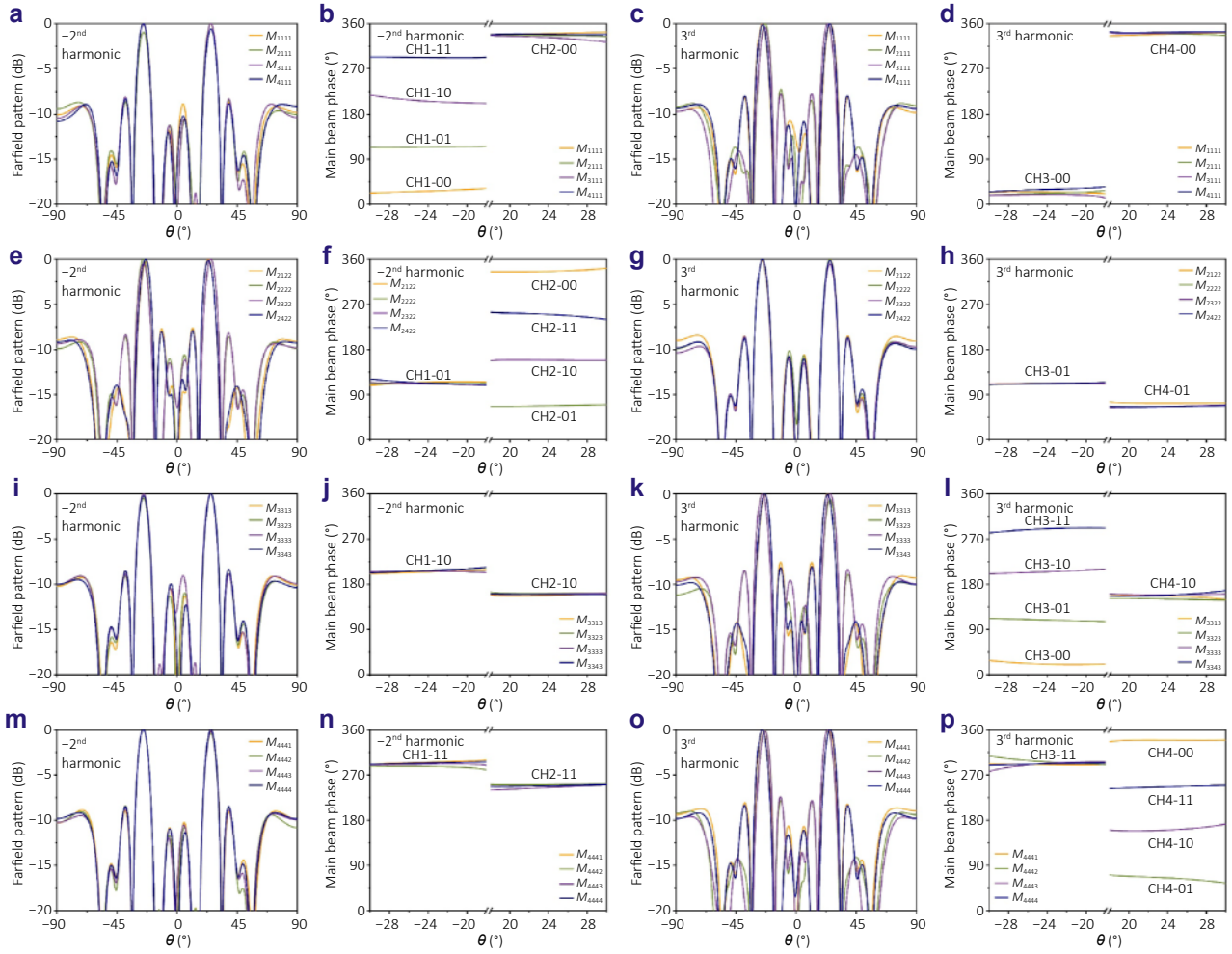


Fig. 5 | Construction of four information transmission channels with independent 2-bit phase modulation capability. (a) Farfield patterns and (b) main beam phases at the −2nd harmonic by applying four STC matrixes $\boldsymbol{M}_{1111}$, $\boldsymbol{M}_{2111}$, $\boldsymbol{M}_{3111}$ and $\boldsymbol{M}_{4111}$. (c) Farfield patterns and (d) main beam phases at the +3rd harmonic by applying four STC matrixes $\boldsymbol{M}_{1111}$, $\boldsymbol{M}_{2111}$, $\boldsymbol{M}_{3111}$ and $\boldsymbol{M}_{4111}$. (e) Farfield patterns and (f) main beam phases at the −2nd harmonic by applying four STC matrixes $\boldsymbol{M}_{2122}$, $\boldsymbol{M}_{2222}$, $\boldsymbol{M}_{2322}$ and $\boldsymbol{M}_{2422}$. (g) Farfield patterns and (h) main beam phases at the +3rd harmonic by applying four STC matrixes $\boldsymbol{M}_{2122}$, $\boldsymbol{M}_{2222}$, $\boldsymbol{M}_{2322}$ and $\boldsymbol{M}_{2422}$. (i) Farfield patterns and (j) main beam phases at the −2nd harmonic by applying four STC matrixes $\boldsymbol{M}_{3313}$, $\boldsymbol{M}_{3323}$, $\boldsymbol{M}_{3333}$ and $\boldsymbol{M}_{3343}$. (k) Farfield patterns and (l) main beam phases at the +3rd harmonic by applying four STC matrixes $\boldsymbol{M}_{3313}$, $\boldsymbol{M}_{3323}$, $\boldsymbol{M}_{3333}$ and $\boldsymbol{M}_{3343}$. (m) Farfield patterns and (n) main beam phases at the −2nd harmonic by applying four STC matrixes $\boldsymbol{M}_{4441}$, $\boldsymbol{M}_{4442}$, $\boldsymbol{M}_{4443}$ and $\boldsymbol{M}_{4444}$. (o) Farfield patterns and (p) main beam phases at the +3rd harmonic by applying four STC matrixes $\boldsymbol{M}_{4441}$, $\boldsymbol{M}_{4442}$, $\boldsymbol{M}_{4443}$ and $\boldsymbol{M}_{4444}$.

utilizing three different harmonics (−1st, 1st, 2nd) and two different beam directions (±24°), and we also discuss the challenges and potential solutions for further increasing the channel number (see Supplementary information of Section 6 for more details). In addition, another four-channel case is also provided to implement BPSK, QPSK and 8PSK modulation schemes respectively at different channels (see Supplementary Section 7 for more details).

2.5 A four-channel wireless communication system and its performance

To vaildate the capability of ASTCM to transmit multiple digital information, we use it to construct a four-channel wireless communication system, whose working mechanism is shown in Fig. 6(a). First, four different original information (named Info.1, Info.2, Info.3 and Info.4) are mapped into four digital bit streams respectively. Then, these digital bit streams are divided into 2-bit forms and subsequently mapped into 2-bit main beam phase streams. According to the above four-channel independent phase modulation method, these four main beam phase streams are interleaved and further converted into STC matrix streams, and output to ASTCM as control signals through MLCC. Incident by a monochromatic carrier wave, ASTCM reflects modulated microwaves carrying the four digital information for space-frequency division multiplexing transmissions. Finally, the four digital information are

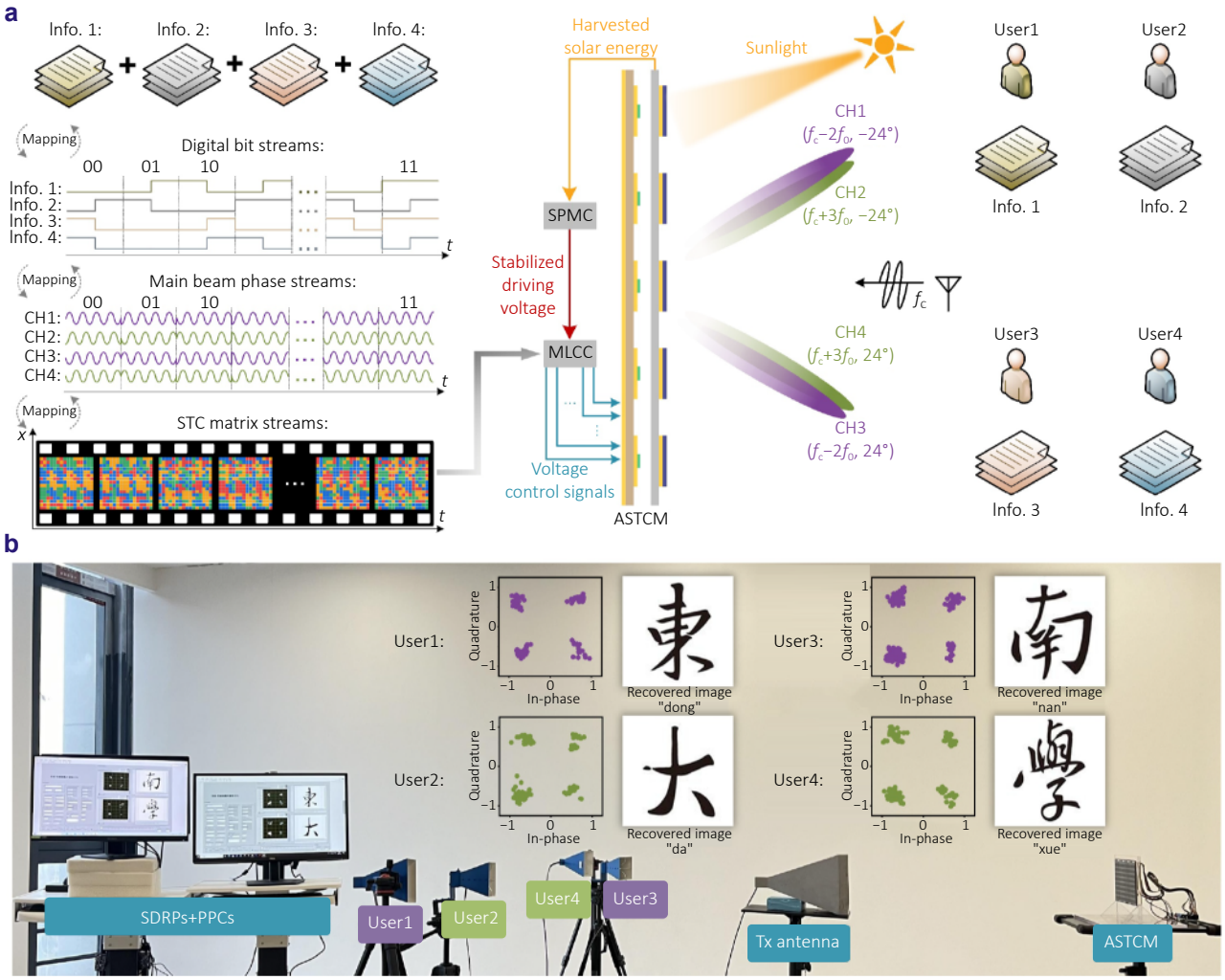


Fig. 6 | The energy self-sufficient four-channel wireless communication system and its performance. (a) The working mechanism of the system. (b) Photograph of the system built in the indoor environment. The insets illustrate the received QPSK constellation diagrams and the recovered images by four user terminals respectively.

respectively received by four distinct user terminals (named User1, User2, User3 and User4) operating at different frequencies and located at different spatial positions. For user terminals in the same spatial position (e.g., User1 and User2), independent information transmission is ensured based on frequency division multiplexing; while for user terminals in different spatial positions but with the same operating frequency (e.g., User1 and User3), independent information transmission is achieved based on space division multiplexing. More importantly, ASTCM in such system demonstrates an autonomous and efficient capacity for harvesting the ambient solar energy, coupled with the feature of low power consumption. Such attributes endow the system to be flexibly deployed in real outdoor scenarios, enabling multi-channel information transmission through autonomous ambient solar energy harvesting even in the absence of power coverage.

As a proof of concept, a realistic four-channel wireless communication system is further built in the indoor environment, as illustrated in Fig. 6(b). The transmitting part of the system is composed of the realized ASTCM (including the SPMC and the MLCC), a transmitting (T_x) horn antenna and a microwave carrier generator (not shown in the figure). The T_x antenna connects the output of the microwave carrier generator and illuminate the unmodulated microwave carrier wave to ASTCM. The receiving system consists of four receiving (R_x) horn antennas, two dual-channel software-defined radio platforms (SDRPs), and two post-processing computers (PPCs). The four R_x antennas act as four user terminals respectively, each of which is connected to a demodulation channel of one SDRP, and the received digital information is processed and displayed through the PPC. In the experiment, we transmitted four black and white images (representing calligraphy of the Chinese characters “东”, “南”, “大” and “学”) to the four user terminals, respectively. The received QPSK constellation

diagrams and the recovered images are shown in the insets of Fig. 6(b). It can be observed that all the received constellation diagrams have four clear constellation points, and the corresponding error vector magnitudes (EVMs) are calculated as 9.55%, 11.86%, 12.65% and 12.06%, respectively, incidating good communication quality of all four channels (see Supplementary information of Section 8 for more details of the measured communication performance). The four recovered images are all error-free, demonstrating that the system has low inerchannel interference characteristics (see Supplementary information of Movie 1 for more details of the four-channel image transmission experiment). Furthermore, we also evaluated the energy efficiency of the system. Considering that the four channels in the current experiment all adopt the QPSK modulation scheme, the information that can be transmitted in one symbol time is 8 bit. In addition, we measured the power consumption of the system during the four-channel image transmission experiment to be 139 mW. Therefore, the energy consumption per bit of the system is calculated as about 17.4 mW/bit. According to the aforementioned ambient energy harvesting performance verification results, it can be inferred that the system can be easily and solely driven by the ambient solar energy harvested by ASTCM. As shown in Table 1, we also compare our system with a series of state-of-the-art PM-based wireless communication systems and find that our system has the smallest energy consumption per bit to date, demonstrating the high energy efficiency of the system. Moreover, although notable progress has been achieved in the realms of dynamic beamforming, direct information modulation as well as energy harvesting and energy self-sufficiency, respectively, our ASTCM-based system pioneers to implement all of the above functionalities on a single platform, reveling its promising potential for advancing next-generation wireless communications (see Supplementary information of Section 9 for more details of the performance comparision).

3 Conclusions

In summary, we reported an innovative ASTCM that is able to manipulate the reflection EM waves in space and frequency domains, and autonomously harvest ambient solar energy by sharing the same physical aperture. On one hand, ASTCM enables independent beamforming at multiple harmonic frequencies simultaneously, and different beamforming experiments are implemented to verify this appealing feature. By harnessing the power of such

Table 1 | Comparison of several state-of-the-art PM-based wireless communication systems in the literature.

Refs.	Metasurface property				System performance			
	Control strategy	Dynamic beamforming	Information modulation	Ambient energy harvesting	Multiplexing method	Channel number	Modulation scheme†	Energy consumption/bit (mW/bit)
ref.[18]	TC	√	√	×	/	1	256QAM	85.2 (PM only)
ref.[24]	SC	√	√	×	SDM	4	Four-channel QPSK	212.5* (PM only)
ref.[26]	SC	√	√	×	SDM	3	Three-channel QPSK	569.6* (PM only)
ref.[27]	SC	√	√	×	SDM	2	Four-channel 64QAM	106 (PM only)
ref.[28]	STC	√	√	×	SFDM	2	Dual-channel OOK	/
ref.[32]	SC	√	√	×	SPDM	2	8PSK & QPSK	5.54 (PM only)
ref.[36]	SC	√	×	√	/	1	QPSK	90 (PM only)
ref.[39]	TC	×	√	√	/	1	16QAM	44.1 (PM+CC)
This work	STC	√	√	√	SFDM	4	Four-channel QPSK	≤ 1.6 (PM only) 17.4 (PM+CC)

TC: time-coding, SC: space-coding, SDM: space division multiplexing, SFDM: space-frequency division multiplexing, SPDM: space-polarization division multiplexing, QAM: quadrature amplitude modulation, OOK: on-off keying, CC: control circuit, †: the highest order modulation scheme implemented by the system, *: estimated value, /: not mentioned.

multi-frequency multi-beamforming and further modulating the phase of each beam, multiple independent information transmission channels can be construct through efficient space-frequency division multiplexing manipulation. On the other hand, the ASTCM achieves full autonomous power supply by virtue of its ability to harvest ambient solar energy and its own low power consumption characteristics, thereby effectively alleviating the over-reliance of traditional PMs on external power supplies. As a proof of concept, we built and tested a four-channel wireless communication system based on ASTCM. The system was proven to be able to transmit four different images to four user terminals simultaneously, independently, and in real time through its four channels using the QPSK modulation scheme. In addition, the system stands out from a number of advanced PM-based wireless communication systems in terms of high energy efficiency, achieving a remarkably low energy consumption per bit of 17.4 mW/bit. The ASTCM innovation provides a simple and effective method to achieve high integration of dynamic beamforming, direct information modulation as well as ambient energy harvesting on a simple physical platform, which is of fundamentally important for achieving high capacity, high energy efficiency and green sustainable development of future wireless communications.

4 Experimental setup

To verify the solar energy harvesting performance of the ASTCM, we built a solar simulator based on two full-spectrum LED lamp beads (LEDGUHON, JH-100WBVG14G45) with a rated power of 100 W. A 60° lens was installed in front of each LED lamp bead to concentrate the radiated light. The solar simulator was placed 20 cm in front of the ASTCM and a programmable DC voltage source (GWINSTEK, GPP-4323(G/L)) was used as a dimmer, allowing the solar radiation irradiance on the surface of the ASTCM to be dynamically controlled from 0 to 100 mW/cm^2. Photograph and spectra of the solar simulator are shown in Fig. S11. In addition, we connected a digital source meter (KEITHLEY, 2450 SourceMeter Instrument) to the ASTCM to measure its real-time *I*-*V* and *P*-*V* responses.

To precisely evaluate the multi-beamforming performance of the ASTCM, we conducted experiments by placing it in a microwave anechoic chamber, thereby effectively eliminating any potential interference stemming from the external environment. A self-made metamaterial lens antenna operating from 5.3 to 15.2 GHz was adopted as the feed antenna to illuminate plane wave on the ASTCM with a distance of 1.5 m[41]. Both the ASTCM and the feed antenna were placed on a turntable, and their relative position remain unchanged whether the turntable rotates. An ultra-wideband standard horn antenna operating from 2 to 18 GHz was used as the receiving antenna and placed 15 m away from the turntable. In each farfield pattern experiment, the turntable rotated from −90° to 90° in steps of 1°. After the turntable rotated one step, the receiving antenna synchronously recorded one RF energy value reflected from ASTCM. Finally, the recorded data were processed into normalized farfield patterns and compared with theoretical calculated values.

To validate the performance of the ASTCM-based four-channel wireless communication system, we placed the above-mentioned metamaterial lens antenna as the T_x antenna at a distance of 1.5 m from ASTCM. The T_x antenna was connected to a microwave carrier generator (RIGOL, DSG3136B), which transmitted an unmodulated microwave carrier signal with a frequency of f_c = 9 GHz. Then, the incident microwave carrier signal was directly converted into four different modulation signals by the ASTCM and transmitted through four different channels (CH1−CH4). In the four-channel image transmission experiment, the STC configuration parameters were set as follows: t_0 =1 μs, L = 16 and f_0 = 62.5 kHz. Since all channel adopted the QPSK modulation scheme, the transmission rate of each channel can be calculated as 250 kbps, and the total transmission rate of the system is therefore 1 Mbps. In addition, we used two dual-channel software radio platforms (NATIONAL INSTRUMENTS, USRP-2954) to provide four independent demodulation channels. Each demodulation channel was connected to a standard horn antenna operating from 8 to 12 GHz, acting as one of four user terminals (User1−User4), and was about 3.5 m away from ASTCM. User1 and User2 were placed at −24° of the ASTCM normal, with operating frequencies of f_{-2} = 8.999875 GHz and f_{+3} = 9.0001875 GHz respectively; User 3 and User 4 are located at 24° of the ASTCM normal, with operating frequencies of f_{-2} = 8.999875 GHz and f_{+3} = 9.0001875 GHz respectively. Therefore, User1−User4 received the image information transmitted in CH1−CH4 respectively. Finally, we used the digital source meter to test the power consumption of the system during four-channel image transmission, and evaluated its energy efficiency and energy self-sufficiency performance accordingly.

References

1. You XH, Wang CX, Huang J et al. Towards 6G wireless communication networks: vision, enabling technologies, and new paradigm shifts. *Sci China Inf Sci* **64**, 110301 (2021).
2. Bariah L, Mohjazi L, Muhaidat S et al. A prospective look: key enabling technologies, applications and open research topics in 6G networks. *IEEE Access* **8**, 174792–174820 (2020).
3. Nguyen DC, Ding M, Pathirana PN et al. 6G internet of things: a comprehensive survey. *IEEE Int Things J* **9**, 359–383 (2022).
4. Chen K, Zhang N, Ding GW et al. Active anisotropic coding metasurface with independent real-time reconfigurability for dual polarized waves. *Adv Mater Technol* **5**, 1900930 (2020).
5. Taravati S, Eleftheriades GV. Full-duplex reflective beamsteering metasurface featuring magnetless nonreciprocal amplification. *Nat Commun* **12**, 4414 (2021).
6. Tian HW, Xu L, Li X et al. Integrated control of radiations and

in-band co-polarized reflections by a single programmable metasurface. *Adv Funct Mater* **33**, 2302753 (2023).
7. Venkatesh S, Lu XY, Saeidi H et al. A high-speed programmable and scalable terahertz holographic metasurface based on tiled CMOS chips. *Nat Electron* **3**, 785–793 (2020).
8. Tian HW, Zhang XG, Jiang WX et al. Programmable controlling of multiple spatial harmonics via a nonlinearly phased grating metasurface. *Adv Funct Mater* **32**, 2203120 (2022).
9. Sun YL, Zhang XG, Huang ZX et al. Intelligent transmissive microwave metasurface with optical sensing and transparency. *Research* **7**, 0514 (2024).
10. Sun SL, He Q, Xiao SY et al. Gradient-index meta-surfaces as a bridge linking propagating waves and surface waves. *Nat Mater* **11**, 426–431 (2012).
11. Jiang GB, Wang YY, Zhang ZY et al. Abnormal beam steering with kirigami reconfigurable metasurfaces. *Nat Commun* **16**, 1660 (2025).
12. Pan CH, Ren H, Wang KZ et al. Reconfigurable intelligent surfaces for 6G systems: principles, applications, and research directions. *IEEE Commun Mag* **59**, 14–20 (2021).
13. Basharat S, Hassan SA, Pervaiz H et al. Reconfigurable intelligent surfaces: potentials, applications, and challenges for 6G wireless networks. *IEEE Wirel Commun* **28**, 184–191 (2021).
14. Liu YW, Liu X, Mu XD et al. Reconfigurable intelligent surfaces: principles and opportunities. *IEEE Commun Surv Tutorials* **23**, 1546–1577 (2021).
15. Basar E, Di Renzo M, De Rosny J et al. Wireless communications through reconfigurable intelligent surfaces. *IEEE Access* **7**, 116753–116773 (2019).
16. Zhao J, Yang X, Dai JY et al. Programmable time-domain digital-coding metasurface for non-linear harmonic manipulation and new wireless communication systems. *Natl Sci Rev* **6**, 231–238 (2019).
17. Dai JY, Tang WK, Yang LX et al. Realization of multi-modulation schemes for wireless communication by time-domain digital coding metasurface. *IEEE Trans Antennas Propagat* **68**, 1618–1627 (2020).
18. Chen MZ, Tang WK, Dai JY et al. Accurate and broadband manipulations of harmonic amplitudes and phases to reach 256 QAM millimeter-wave wireless communications by time-domain digital coding metasurface. *Natl Sci Rev* **9**, nwab134 (2022).
19. Cui TJ, Liu S, Bai GD et al. Direct transmission of digital message via programmable coding metasurface. *Research* **2019**, 2584509 (2019).
20. Zhang XG, Sun YL, Zhu BC et al. A metasurface-based light-to-microwave transmitter for hybrid wireless communications. *Light Sci Appl* **11**, 126 (2022).
21. Zheng YL, Xu ZY, Zhang N et al. Spatial-division-assisted multi-level amplitude-programmable metasurface for dual-band direct wireless communication. *Adv Mater Technol* **8**, 2201654 (2023).
22. Wu RY, He S, Wu JW et al. Multi-frequency amplitude-programmable metasurface for multi-channel electromagnetic controls. *Nanophotonics* **12**, 2433–2442 (2023).
23. Xiong Q, Zhang ZJ, Huang C et al. Amplitude-phase independently encoding space-division multiplexed wireless communication using beamforming reconfigurable metasurfaces. *Adv Opt Mater* **12**, 2401181 (2024).
24. Wan X, Xiao CK, Huang H et al. Joint modulations of electromagnetic waves and digital signals on a single metasurface platform to reach programmable wireless communications. *Engineering* **8**, 86–95 (2022).
25. Xiong Q, Zhang ZJ, Ma XL et al. Multi-channel wireless communication based on amplitude-phase reconfigurable space-coding beamforming metasurface. *Adv Electron Mater* **10**, 2400056 (2024).
26. Zhao HT, Shuang Y, Wei ML et al. Metasurface-assisted massive backscatter wireless communication with commodity Wi-Fi signals. *Nat Commun* **11**, 3926 (2020).
27. Xu H, Wu JW, Wang ZX et al. Two-dimensional and high-order directional information modulations for secure communications based on programmable metasurface. *Nat Commun* **15**, 6140 (2024).
28. Zhang L, Chen MZ, Tang WK et al. A wireless communication scheme based on space-and frequency-division multiplexing using digital metasurfaces. *Nat Electron* **4**, 218–227 (2021).
29. Wu GB, Dai JY, Shum KM et al. A universal metasurface antenna to manipulate all fundamental characteristics of electromagnetic waves. *Nat Commun* **14**, 5155 (2023).
30. Ke JC, Chen XY, Tang WK et al. Space-frequency-polarization-division multiplexed wireless communication system using anisotropic space-time-coding digital metasurface. *Natl Sci Rev* **9**, nwac225 (2022).
31. Zhang L, Cui TJ. Space-time-coding digital metasurfaces: principles and applications. *Research* **2021**, 9802673 (2021).
32. Wang ZX, Wu JW, Xu H et al. A dual-polarization programmable metasurface for green and secure wireless communication. *Adv Sci* **11**, 2403624 (2024).
33. Ma Q, Hong QR, Gao XX et al. Highly integrated programmable metasurface for multifunctions in reflections and transmissions. *APL Mater* **10**, 061113 (2022).
34. Kossifos KM, Georgiou J, Antoniades MA. ASIC-enabled programmable metasurfaces-Part 1: design and characterization. *IEEE Trans Antennas Propagat* **72**, 2790–2799 (2024).
35. Kossifos KM, Georgiou J, Antoniades MA. ASIC-enabled programmable metasurfaces-Part 2: performance and synthesis. *IEEE Trans Antennas Propagat* **72**, 2800–2810 (2024).
36. Chang MY, Mu YJ, Han JQ et al. Tailless information–energy metasurface. *Adv Mater* **36**, 2313697 (2024).
37. Mu YJ, Chang MY, Wang X et al. A self-powered reconfigurable intelligent metasurface. *Adv Mater Technol* **9**, 2301896 (2024).
38. Ruan Y, Nie QF, Chen L et al. Optical transparent and reconfigurable metasurface with autonomous energy supply. *J Phys D Appl Phys* **53**, 065301 (2020).
39. Tian HW, Sun YL, Zhang XG et al. Solar-powered light-modulated microwave programmable metasurface for sustainable wireless communications. *Nat Commun* **16**, 2524 (2025).
40. Hao YJ, Niu ZH, Yang JY et al. Self-powered terahertz modulators based on metamaterials, liquid crystals, and triboelectric nanogenerators. *ACS Appl Mater Interfaces* **16**, 32249–32258 (2024).
41. Tian HW, Jiang WX, Li X et al. An ultrawideband and high-gain antenna based on 3-D impedance-matching metamaterial lens. *IEEE Trans Antennas Propagat* **69**, 3084–3093 (2021).

Acknowledgements

This work is supported by the National Science Foundation of China (U23B2015, 62288101, 62501149), the Natural Science Foundation of Jiangsu Province (BK20251323), the Fundamental Research Funds for the Central Universities (2242023K5002), the 111 Project (111-2-05) and the Postdoctoral Fellowship Program of China Postdoctoral Science Foundation (GZB20250145).

Author contributions

H.W.T., T.J.C. and W.X.J. conceived the idea. H.W.T. performed theoretical analyses and numerical simulations. H.W.T., C.S., D.J.W. and Q.Z. performed experimental measurements. H.W.T. evaluated the experimental and numerical results. H.W.T., T.J.C. and W.X.J. wrote the manuscript. T.J.C. and W.X.J. guided the research. All the authors contributed to the discussions of the results and the manuscript preparation.

Competing interests

The authors declare no competing financial interests.

Supplementary information

Supplementary information for this paper is available at https://doi.org/10.29026/oea.2026.250229

Open Access This article is licensed under a Creative Commons Attribution 4.0 International License, which permits use, sharing, adaptation, distribution and reproduction in any medium or format, as long as you give appropriate credit to the original author(s) and the source, provide a link to the Creative Commons license, and indicate if changes were made. To view a copy of this license, visit http://creativecommons.org/licenses/by/4.0/
©The Author(s) 2026.
Published by Editorial Office of *Opto-Electronic Advance*, Institute of Optics and Electronics, Chinese Academy of Sciences.

Opto-Electronic Journals Group
www.oejournal.org
Scan for Article PDF